

Quintom Dark Energy: Future Attractor and Phantom Crossing in Light of DESI DR2 Observation

Phusuda Thanankullaphong,^{1,*} Prasanta Sahoo,^{2,1,†}
Prajwal Hassan Puttasiddappa,^{3,4,5,‡} and Nandan Roy^{1,§}

¹*NAS, Centre for Theoretical Physics & Natural Philosophy, Mahidol University, Nakhonsawan Campus, Phayuha Khiri, Nakhonsawan 60130, Thailand*

²*Midnapore College (Autonomous), Midnapore, West Bengal, India, 721101*

³*PPGCosmo, Universidade Federal do Espírito Santo, 29075-910, Vitória, ES, Brazil*

⁴*Departamento de Física Teórica, Instituto de Física, Universidade do Estado do Rio de Janeiro (UERJ), Rua São Francisco Xavier 524, Maracana CEP 20550-013, Rio de Janeiro, RJ, Brazil*

⁵*Institute of Theoretical Astrophysics, University of Oslo, Sem Sælands vei 13, 0371 Oslo, Norway*

We study the late-time cosmological dynamics of a two-field dark energy model consisting of a canonical quintessence scalar field and a phantom scalar field in a spatially flat FLRW universe. The fields are minimally coupled to gravity and uncoupled at the level of the potential, with the quintessence sector governed by an exponential potential and the phantom sector by an inverse power-law potential. By reformulating the background equations as a five-dimensional autonomous dynamical system, we identify and analyze the fixed points and their stability properties, revealing stable late-time attractors corresponding to phantom-dominated accelerated expansion. We confront the model with observations through a Bayesian parameter estimation performed using the COBAYA framework, employing several combinations of recent cosmological data sets, including Pantheon+ supernovae, compressed cosmic microwave background distance priors, DESI DR2 baryon acoustic oscillation measurements, and DES Year-5 supernova data. The observational constraints favor a dynamical dark energy sector moderately and are consistent with deviations from a cosmological constant at the present epoch. The regions of parameter space preferred by the data are compatible with the stable accelerating solutions identified in the dynamical analysis, establishing a direct connection between phase-space stability and observational viability. A notable feature of the model is that the effective dark energy equation of state undergoes phantom divide crossing in a gradual and asymptotic manner, rather than as a sharp transition.

I. INTRODUCTION

Two major tensions in contemporary cosmology involve discrepancies in the measured values of the Hubble constant (H_0) and the amplitude of matter clustering (σ_8), as inferred from different cosmological observations. Early-time probes, including the Cosmic Microwave Background (CMB) [1], Baryon Acoustic Oscillations (BAO) [2], Big Bang Nucleosynthesis (BBN) [3], DES [4], estimate H_0 to lie within $67 - 68.5$ km/s/Mpc. These values are significantly lower, up to a 5.3σ discrepancy, than late-time measurements from SH0ES [5] and H0LiCOW [6], which find $H_0 = 74.03 \pm 1.42$ km/s/Mpc [7]. The parameter σ_8 , quantifies the root-mean-square

of matter density fluctuations at a scale of $8 h^{-1}$ Mpc. A related parameter, $S_8 = \sigma_8 \sqrt{\Omega_m/0.3}$, is often used. Low-redshift probes, such as galaxy clustering, weak gravitational lensing, and galaxy cluster counts[8–12], systematically yield lower S_8 values compared to those derived from primary CMB anisotropies and the CMB lensing power spectrum, with a persistent $2 - 3\sigma$ tension [13].

A recent challenge comes from the Dark Energy Spectroscopic Instrument (DESI), which, through full-shape analysis of scale-dependent clustering of matter, suggests that dark energy may evolve with redshift rather than being a cosmological constant [14–20]. Furthermore, in [20], combinations of these (first year) DESI clustering observations with cosmic microwave background (CMB) data from Planck, CMB lensing from Planck and ACT, Big Bang Nucleosynthesis (BBN) constraints on the baryon density, galaxy weak lensing and clustering from DESY3, and supernovae from DESY5 were shown to

* phusuda.tha@student.mahidol.ac.th

† prasantmath123@yahoo.com

‡ prajwal.puttasiddappa@edu.ufes.br

§ nandan.roy@mahidol.ac.th (Corresponding Author)

support general relativity while favoring a dynamical dark energy model with Chevallier–Polarski–Linder (CPL) equation of state parameters, $w_0 \neq -1$ and $w_a \neq 0$. However, the widely used CPL parameterization may be too simplistic to robustly probe the underlying microphysics of dark energy [21–24]. Quintessence model with a thawing potential can, however, marginally accommodate these observations when mapped onto CPL parameters [25–27].

The inferred CPL parameters further suggest a dynamical dark energy equation of state (EoS) that crosses the phantom divide ($w = -1$), transitioning from $w < -1$ at higher redshifts to $w > -1$ today, with the crossing at $z_{\text{cross}} \sim 0.4\text{--}0.5$ [28, 29] (see also nonparametric reconstructions in [30]). However, the statistical significance typically exceeds 2σ but remains below the 5σ discovery threshold, rendering it inconclusive [31]. This apparent preference may partly reflect the uneven redshift coverage in the data or statistical fluctuations. Indeed, the inferred phantom behaviour could arise as an artefact of extrapolating the linear $w(a)$ form beyond the well-constrained redshift range, while the underlying equation of state stays non-phantom throughout cosmic history [21, 25–27, 32].

It is well established that these features cannot be accommodated within standard Λ CDM or single field quintessence models. Quintom models, consisting of two scalar fields, one canonical (quintessence-like) and one phantom like are therefore well motivated, as they allow the dark energy equation of state $w(z)$ to cross the phantom divide $w = -1$ [33–37] (see [38] for a review). This has attracted significant recent interest, particularly in light of observational indications favouring dynamical dark energy and plausible phantom divide crossing [37, 39–45]. In this work, we construct a quintom dark energy model where both fields are minimally coupled to gravity and interacting only through the background dynamics. An exponential potential governs the quintessence field, while a power-law potential governs the phantom field. Their combined dynamics can allow the equation of state to cross the phantom divide. We have performed a detailed dynamical system analysis of this model by finding the fixed points and their corresponding stability. Finally, we compare the model with current cosmological data to constrain its parameters and assess its observational viability.

The rest of this paper is structured as follows.

After briefly reviewing the no-go theorem for stable phantom crossing in single-field dark energy models and highlighting the advantages of quintom scenarios, we introduce our model and derive the equations governing the background evolution in Sec. II. In Sec. III we introduce the corresponding dynamical system. The fixed points of this system and their stability properties are examined in Sec. IV. In Sec. V, we investigate the evolution of various cosmological and cosmographic parameters, including a statefinder analysis. Sec. VI describes the observational datasets and statistical techniques employed in this work. The resulting constraints from our data analysis are reported in Sec. VII, and we close with a summary and outlook in Sec. VIII.

II. PHANTOM DIVIDE CROSSING AND QUINTOM MODEL

A. Impossibility of Stable Phantom Crossing in Single-Field Models

A transition of the dark energy equation-of-state parameter through $w = -1$ is strongly constrained by fundamental consistency conditions. To illustrate this, consider a single scalar degree of freedom ϕ minimally coupled to gravity, with a general Lagrangian density

$$\mathcal{L} = F(X, \phi), \quad X \equiv \frac{1}{2} \nabla_\mu \phi \nabla^\mu \phi. \quad (1)$$

The associated energy density and pressure are

$$\rho = 2XF_X - F, \quad p = F, \quad (2)$$

yielding the effective equation of state

$$w = \frac{p}{\rho} = \frac{F}{2XF_X - F}. \quad (3)$$

Reaching the phantom divide $w = -1$ requires the condition $F_X = 0$. However, the propagation of scalar fluctuations is governed by the adiabatic sound speed,

$$c_s^2 \equiv \frac{\partial p / \partial X}{\partial \rho / \partial X} = \frac{F_X}{F_X + 2XF_{XX}}. \quad (4)$$

At the would-be crossing point, the sound speed vanishes, while in the phantom regime $F_X < 0$ implies $c_s^2 < 0$. The latter leads to exponential growth of short-wavelength perturbations, rendering the background solution dynamically unstable.

This obstruction is generic and does not depend on the detailed form of $F(X, \phi)$. Canonical quintessence, phantom scalar fields, and k -essence constructions all fail to realize a stable crossing within a single-field description. This constitutes a robust no-go result for phantom divide crossing with one propagating scalar degree of freedom.

B. Role of Multiple Degrees of Freedom

A minimal resolution is obtained by extending the dark energy sector to include more than one scalar mode. In the quintom framework considered here, the effective Lagrangian takes the form

$$\mathcal{L} = X_\phi - X_\sigma - V(\phi, \sigma), \quad (5)$$

where ϕ is canonical and σ carries a negative kinetic term. Each field separately obeys

$$w_\phi > -1, \quad w_\sigma < -1, \quad (6)$$

while the total dark energy equation of state,

$$w_{\text{DE}} = \frac{p_\phi + p_\sigma}{\rho_\phi + \rho_\sigma}, \quad (7)$$

is free to evolve smoothly across $w = -1$. The crossing is controlled by the relative contribution of the kinetic sectors and does not require either field to violate its individual stability bound.

It is worth emphasizing that the two-field quintom model is not the only viable approach to achieving phantom divide crossing. A combination of standard and negative quintessence was also shown to feature phantom divide crossing [45]. Alternative realizations include single-field models with non-canonical (e.g., k -essence) or higher-derivative kinetic terms in the Horndeski class [46–49], hessence models based on a complex scalar field with internal degrees of freedom [50], braneworld scenarios [51], modified gravity theories like $f(R)$ gravity [52, 53], interacting dark energy models [54–56].

C. The Model

We consider a universe that is spatially flat and has both a canonical and a phantom scalar field representing the dark energy sector. Then the Friedmann and acceleration equations are:

$$H^2 = \frac{\kappa^2}{3} \left(\rho_m + \frac{1}{2} \dot{\phi}^2 - \frac{1}{2} \dot{\sigma}^2 + V(\phi, \sigma) \right), \quad (8)$$

$$\dot{H} = -\frac{\kappa^2}{2} \left(\rho_m + \dot{\phi}^2 - \dot{\sigma}^2 \right). \quad (9)$$

Here, $\kappa^2 = 8\pi G$, with $H = \dot{a}/a$ denoting the Hubble function and $a(t)$ representing the scale factor. The quantities related to matter, radiation, quintessence, and the phantom will be denoted through respective subscripts m , r , ϕ , and σ , and the overdots indicate differentiation with respect to the cosmic time.

We consider a simple non-interacting scenario where the potential $V(\phi, \sigma) = V(\phi) + V(\sigma)$. Hence, we have standard continuity equations $\dot{\rho}_i = -3H(p_i + \rho_i)$ for each species $i \in \{m, r, \phi, \sigma\}$. The Klein-Gordon equation for the scalar fields can be expressed as follows:

$$\ddot{\phi} + 3H\dot{\phi} + \frac{dV(\phi)}{d\phi} = 0, \quad (10)$$

$$\ddot{\sigma} + 3H\dot{\sigma} - \frac{dV(\sigma)}{d\sigma} = 0, \quad (11)$$

In this work, we adopt the following scalar-field potentials:

$$\begin{aligned} V(\phi) &= V_{\phi 0} e^{-\lambda_\phi \phi}, \\ V(\sigma) &= M^{4+m}(\sigma)^{-m} \quad (\text{with } m > 0). \end{aligned} \quad (12)$$

The steep exponential potential for the quintessence field does not support slow-roll evolution and therefore keeps the field subdominant at early times and becomes dynamical at late times. Such potentials constitute a standard realization of thawing dark energy models, in which the equation of state w remains close to -1 during the matter-dominated era and subsequently evolves toward less negative values at late times [18, 57, 58]. The phantom field is governed by an inverse power-law potential, which becomes naturally flat for large field values and admits a late-time attractor solution. Power-law potentials for phantom fields are particularly well motivated, as they can give rise to tracker behavior, thereby reducing sensitivity to

initial conditions [36, 59]. Unlike Ref. [60], where direct power-law potentials were considered, here we focus on inverse power-law forms. Such potentials also arise in supersymmetric constructions involving phantom degrees of freedom [61, 62].

D. Linear Scalar Perturbations

We now briefly comment on perturbative behavior of the model. Scalar perturbations around a spatially flat FLRW background can be described in the conformal Newtonian gauge,

$$ds^2 = a^2(\tau) [(1+2\Phi)d\tau^2 - (1-2\Phi)\delta_{ij}dx^i dx^j], \quad (13)$$

where the equality of the metric potentials follows from the absence of anisotropic stress.

For each scalar component $i \in \{\phi, \sigma\}$, the linearized energy conservation equations take the form [37, 63]

$$\dot{\delta}_i = -(1+w_i)(\theta_i - 3\dot{\Phi}) - 3\mathcal{H}(c_{s,i}^2 - w_i)\delta_i, \quad (14)$$

$$\dot{\theta}_i = -\mathcal{H}(1-3w_i)\theta_i - \frac{\dot{w}_i}{1+w_i}\theta_i + \frac{c_{s,i}^2}{1+w_i}k^2\delta_i + k^2\Phi. \quad (15)$$

Unlike single-field models, no divergence arises at $w_{\text{DE}} = -1$, since neither ϕ nor σ individually crosses the phantom boundary. The effective dark energy perturbations are obtained through energy-weighted combinations [35],

$$\delta_{\text{DE}} = \frac{\rho_\phi\delta_\phi + \rho_\sigma\delta_\sigma}{\rho_\phi + \rho_\sigma}, \quad (16a)$$

$$\theta_{\text{DE}} = \frac{(\rho_\phi + p_\phi)\theta_\phi + (\rho_\sigma + p_\sigma)\theta_\sigma}{\rho_\phi + p_\phi + \rho_\sigma + p_\sigma}. \quad (16b)$$

It has been shown in [35, 37], in a set up like ours, both fields propagate with unit sound speed, $c_{s,\phi}^2 = c_{s,\sigma}^2 = 1$, ensuring the absence of gradient instabilities. Consequently, the effective perturbations remain finite through the phantom divide, allowing a consistent realization of phantom crossing at the perturbation level.

III. THE DYNAMICAL SYSTEM

To understand the phase-space behaviour of the system, one needs to introduce a new set of dimensionless variables to write it as an autonomous system. Here we consider the following set of dimensionless transformations:

$$x_\phi^2 = \frac{\kappa^2\dot{\phi}^2}{6H^2}, \quad y_\phi^2 = \frac{\kappa^2V(\phi)}{3H^2}, \quad (17)$$

$$x_\sigma^2 = \frac{\kappa^2\dot{\sigma}^2}{6H^2}, \quad y_\sigma^2 = \frac{\kappa^2V(\sigma)}{3H^2}, \quad (18)$$

$$\lambda_\phi = -\frac{1}{\kappa V(\phi)} \frac{dV(\phi)}{d\phi}, \quad \lambda_\sigma = -\frac{1}{\kappa V(\sigma)} \frac{dV(\sigma)}{d\sigma}. \quad (19)$$

With the help of the above transformations, the background field equations can be reduced to a set of autonomous equations for the choice of the potentials mentioned before:

$$x'_\phi = -3x_\phi + \sqrt{\frac{3}{2}}\lambda_\phi y_\phi^2 + \frac{3}{2}x_\phi \mathcal{U}, \quad (20a)$$

$$x'_\sigma = -3x_\sigma - \sqrt{\frac{3}{2}}\lambda_\sigma y_\sigma^2 + \frac{3}{2}x_\sigma \mathcal{U}, \quad (20b)$$

$$y'_\phi = -\sqrt{\frac{3}{2}}\lambda_\phi x_\phi y_\phi + \frac{3}{2}y_\phi \mathcal{U}, \quad (20c)$$

$$y'_\sigma = -\sqrt{\frac{3}{2}}\lambda_\sigma x_\sigma y_\sigma + \frac{3}{2}y_\sigma \mathcal{U}, \quad (20d)$$

$$\lambda'_\sigma = -\sqrt{6}\lambda_\sigma^2 x_\sigma \left(\frac{1}{m}\right), \quad (20e)$$

$$\text{where, } \mathcal{U} = (1 + x_\phi^2 - x_\sigma^2 - y_\phi^2 - y_\sigma^2). \quad (20f)$$

The prime is the differentiation with respect to $N = \ln a$. Different cosmological variables can be expressed in terms of the dynamical system variables as follows,

$$\Omega_\phi = x_\phi^2 + y_\phi^2, \quad \Omega_\sigma = -x_\sigma^2 + y_\sigma^2, \quad (21)$$

$$\Omega_{\text{DE}} = x_\phi^2 - x_\sigma^2 + y_\phi^2 + y_\sigma^2, \quad (22)$$

$$w_\phi = \frac{x_\phi^2 - y_\phi^2}{x_\phi^2 + y_\phi^2}, \quad w_\sigma = \frac{-x_\sigma^2 - y_\sigma^2}{-x_\sigma^2 + y_\sigma^2}, \quad (23)$$

$$w_{\text{DE}} \equiv \frac{p_{\text{DE}}}{\rho_{\text{DE}}} = \frac{x_\phi^2 - x_\sigma^2 - y_\phi^2 - y_\sigma^2}{x_\phi^2 - x_\sigma^2 + y_\phi^2 + y_\sigma^2}, \quad (24)$$

$$q = -1 + \frac{3}{2}(1 + x_\phi^2 - x_\sigma^2 - y_\phi^2 - y_\sigma^2). \quad (25)$$

Here, Ω_ϕ , Ω_σ and Ω_{DE} represents the quintessence, phantom and total dark energy density parameter respectively with w_ϕ , w_σ and w_{DE} as the corresponding equation of state while q is the universe's deceleration parameter. In the next section, we analyze the fixed points and their stability.

IV. FIXED POINTS AND STABILITY

The fixed points of the system are determined by solving Eq. (20) with all derivatives with respect to N set to zero. The resulting fixed points and their associated eigenvalues are summarized in Table I. The corresponding physical characteristics of these fixed points are provided in Table II.

The stability of a fixed point in a nonlinear system is determined by the eigenvalues of the Jacobian matrix evaluated at that point. When all the eigenvalues have non-zero real parts (i.e., the fixed point is hyperbolic), linear stability analysis can be directly applied. However, in the case of non-hyperbolic fixed points, where one or more eigenvalues have zero real parts, stability must be analysed using analytical tools such as the centre manifold theorem or suitable numerical techniques. For a review on the dynamical systems in cosmology, see [64].

The fixed points p_1 and p_2 correspond to matter-dominated solutions with $\Omega_m = 1$ and the value of the deceleration parameter at these fixed points is $q = \frac{1}{2}$. Although these points are non-hyperbolic due to the presence of a zero eigenvalue associated with the λ_σ direction, the coexistence of both positive and negative eigenvalues indicates that they are saddle points in phase space, as expected for a transient matter-dominated epoch. The point p_2 represents a degenerate extension of p_1 , containing it as a subset, and does not correspond to a physically distinct cosmological phase.

The fixed point p_3 represents a universe dominated by the kinetic energy of the quintessence field, with $x_\phi = \pm 1$. In this regime, the scalar field behaves as a stiff fluid with equation of state $w = 1$, leading to strong deceleration ($q = 2$). This point is unstable and corresponds to an early-time kinetic-dominated phase for the quintessence scalar field.

The fixed point p_4 corresponds to a mixed scaling solution in which the quintessence field and matter coexist. In this case, the effective equation of state of the quintessence field coincides with that of matter, $w_\phi = 0$, making the scalar field dynamically indistinguishable from dust. This point is decelerating and unstable, and therefore can only represent a transient phase of the cosmic evolution.

The fixed point p_5 describes another mixed configuration involving the quintessence field. Although this point can yield accelerated expansion for $\lambda_\phi^2 < 2$, it possesses both positive and negative eigenvalues and is therefore a saddle point. Consequently, despite allowing for acceleration, it cannot act as a late-time attractor.

The fixed point p_6 is characterized by complete domination of the potential energy of the phantom field, with $y_\sigma = \pm 1$. This solution corresponds to a de Sitter-like accelerated phase with $w = -1$ and $q = -1$. The eigenvalue spectrum consists of three negative eigenvalues and two vanishing eigenvalues, rendering the point non-hyperbolic. Consequently, linear stability analysis alone is insufficient to establish its asymptotic behaviour.

To assess the stability of p_6 , we investigate the phase-space trajectories numerically by constructing two-dimensional projections involving y_σ and the remaining dynamical variables. The resulting phase portraits, shown in Fig. 1, demonstrate that trajectories in the physically relevant subregion of phase space are attracted toward $y_\sigma = \pm 1$. This indicates that p_6 behaves as a stable late-time attractor in full phase space at the level of background dynamics.

The fixed point p_7 represents a special case of the scaling solution p_4 , corresponding to a restricted subspace of the full phase space. Although p_7 can be formally treated as a separate critical point, it shares the same physical interpretation, cosmological properties, and stability behaviour as p_4 .

The fixed point p_8 corresponds to complete kinetic domination by both the quintessence and phantom fields. Despite the presence of zero eigenvalues, the positive eigenvalues render this point unstable. Since the effective equation of state is again $w = 1$, this solution always leads to decelerated expansion and cannot describe either late-time acceleration or a viable matter-dominated epoch.

The fixed point p_9 corresponds to a special case of the nondegenerate fixed point p_5 , obtained by restricting the system to $\lambda_\sigma = 0$. Its phase-space co-

ordinates, cosmological parameters, and eigenvalue structure coincide with those of p_5 . Consequently, p_9 represents the same physical configuration, namely a quintessence-dominated universe that can exhibit accelerated expansion for $\lambda_\phi^2 < 2$, but which is dynamically unstable due to the presence of positive eigenvalues. As in the case of p_5 , this fixed point can at most describe a transient accelerating phase and cannot act as a late-time attractor.

The dynamical systems analysis performed here reveals that, among all fixed points of the model, only the phantom potential-dominated solution p_6 can act as a late-time attractor capable of driving cosmic acceleration. All other fixed points correspond to either decelerated or unstable phases and therefore represent transient stages in the cosmic evolution.

V. COSMOLOGICAL EVOLUTION AND STATEFINDER ANALYSIS

In this section, we discuss the cosmological evolution of the quintom model and analyze its dynamical properties using the statefinder diagnostic. The discussion is based on Figs. 2–3, obtained by numerically integrating the full background equations. Though in the dynamical system analysis in the previous section, we have not included radiation since we are interested in the late-time dynamics, but to solve the system of equations numerically, we have considered radiation in the system and have set the initial condition in the radiation-dominated era, such that we can obtain all the cosmological eras properly.

To reproduce a dark energy equation of state (EoS) crossing the phantom divide in the recent past, with the EoS evolving from the phantom regime to the quintessence regime, we require the effective EoS to start in the phantom region at early times. This can be achieved by choosing initial conditions such that $x_{\phi_i} < x_{\sigma_i}$, while keeping all other dynamical system variables of the same order of magnitude. In addition, the condition $x_{\sigma_i} < y_{\sigma_i}$ must be satisfied to ensure that the phantom field energy density remains physical.

Subject to these requirements, we adopt the following initial conditions at $N = -8.5$: $x_{\phi_i} = 0.2 \times 10^{-7}$, $x_{\sigma_i} = 0.1 \times 10^{-5}$, $y_{\phi_i} = 0.35 \times 10^{-5}$, $y_{\sigma_i} = 0.2 \times 10^{-5}$, $\lambda_{\sigma_i} = 0.05$, $\Omega_r = 0.999$. We have verified that the qualitative behaviour of the system remains unchanged under small variations of these

initial conditions. The values of λ_ϕ are chosen in accordance with the constraints obtained from the MCMC analysis presented in the next section. For all the plots and the MCMC analysis presented here we have considered $m = 4$.

A. Background Evolution and Phantom Crossing

Fig. 2a shows the evolution of the density parameters Ω_m , Ω_r , and Ω_{DE} , together with Ω_ϕ and Ω_σ , as functions of the e-folding number $N = \ln a$ for three representative values of the quintessence slope parameter $\lambda_\phi = \{1, 1.5, 2\}$. The universe exhibits the standard sequence of cosmological epochs, beginning with radiation domination, followed by a prolonged matter-dominated era, and finally transitioning to dark-energy domination at late times. It can also be seen that the present day values of the density parameters inferred from these plots are consistent with the posterior constraints obtained in the next section. The evolution of the dimensionless variables x_ϕ , x_σ , y_ϕ , and y_σ is shown in Fig. 2b.

In Fig. 2c, we plot the evolution of the equations of state of the scalar fields, (w_ϕ, w_σ) , together with the total dark energy equation of state, w_{DE} , for the same values of λ_ϕ used in the density parameter plot. For the choice of initial conditions specified earlier, w_{DE} initially lies in the phantom regime, rapidly approaches $w_{\text{DE}} \simeq -1$, and remains nearly constant throughout the matter-dominated era. With the onset of dark-energy domination, w_{DE} becomes dynamical and evolves into the quintessence regime, crossing the phantom divide. In future, it asymptotically returns to $w_{\text{DE}} \simeq -1$, effectively mimicking a cosmological constant.

From Fig. 2b, we observe that the quintessence field is frozen in the early universe, becomes dynamical at late times during the onset of dark-energy domination, and freezes again in the future. Both the kinetic (x_ϕ) and potential (y_ϕ) contributions of the quintessence field asymptotically vanish. In contrast, the phantom field becomes dynamical at late times, and in the asymptotic future the universe is dominated by the phantom sector with $y_\sigma \simeq 1$. This behavior confirms our dynamical system analysis in the previous section, which predicts a single late-time attractor dominated by the phantom field.

It is worth noting, however, that although the total dark energy equation of state w_{DE} starts in

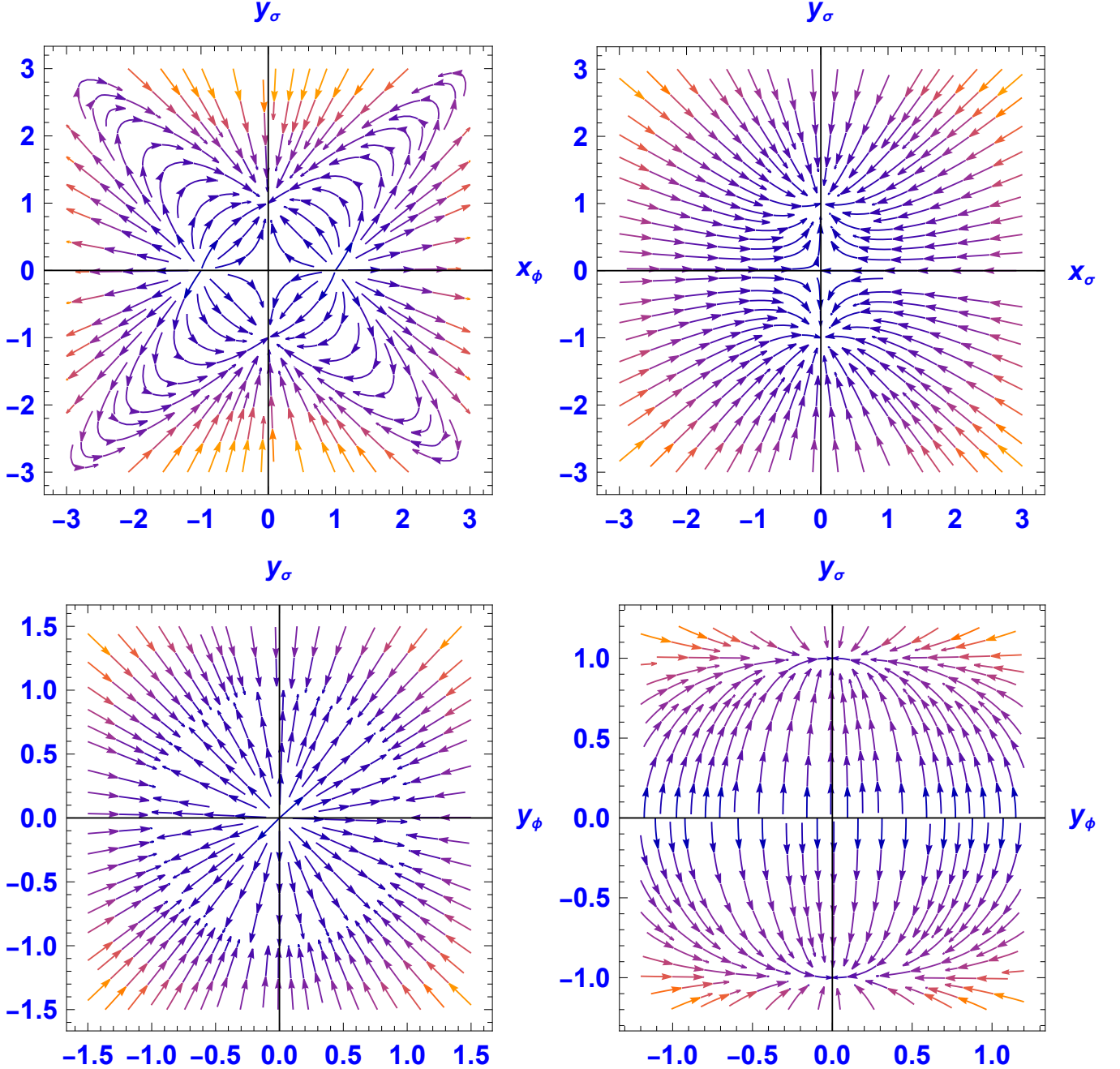


FIG. 1: The two-dimensional projected phase spaces for the fixed point p_6 involving y_σ as one dimension and the remaining dynamical variables as another dimension.

the phantom regime in the very early universe, the visible phantom divide crossing occurs at $z \simeq 1-4$. According to the current model, the phantom crossing may therefore occur earlier than suggested by the DESI DR2 observations. Moreover, the crossing takes place gradually and asymptotically, rather than as a sharp transition[23, 63, 65]. At first glance, this behavior might appear to be an artifact of the chosen initial conditions or scalar-field potentials.

However, its robustness is supported by the dynamical systems analysis presented in the previous section.

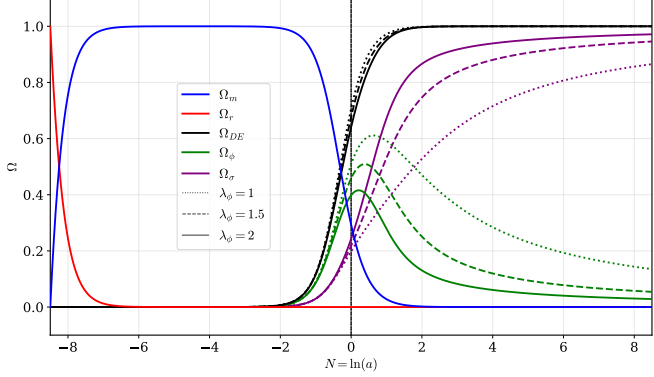
For a quintom model to successfully reproduce the standard sequence of cosmological epochs, it must pass through a prolonged matter-dominated phase. The fixed points corresponding to matter domination, $\Omega_m \rightarrow 1$, are generically saddle points, characterized by $x_i \rightarrow 0$ and $y_i \rightarrow 0$, as also re-

Fixed Point	x_ϕ	x_σ	y_ϕ	y_σ	λ_σ	Eigenvalues
p_1	0	0	0	0	0	$\left\{-\frac{3}{2}, -\frac{3}{2}, \frac{3}{2}, \frac{3}{2}, 0\right\}$
p_2	0	0	0	0	-	$\left\{-\frac{3}{2}, -\frac{3}{2}, \frac{3}{2}, \frac{3}{2}, 0\right\}$
p_3	± 1	0	0	0	-	$\left\{3, 3, 0, 0, \frac{1}{2}(\sqrt{6}\lambda_\phi \mp 6)\right\}$
p_4	$\frac{\sqrt{3/2}}{\lambda_\phi}$	0	$\pm \frac{\sqrt{3/2}}{\lambda_\phi}$	0	-	$\left\{0, -\frac{3}{2}, \frac{3}{2}, \frac{3(-\lambda_\phi^2 - \sqrt{24\lambda_\phi^2 - 7\lambda_\phi^4})}{4\lambda_\phi^2}, \frac{3(\sqrt{24\lambda_\phi^2 - 7\lambda_\phi^4} - \lambda_\phi^2)}{4\lambda_\phi^2}\right\}$
p_5	$\frac{\lambda_\phi}{\sqrt{6}}$	0	$\pm \frac{\sqrt{6 - \lambda_\phi^2}}{\sqrt{6}}$	0	-	$\left\{0, \frac{\lambda_\phi^2}{2}, \frac{1}{2}(\lambda_\phi^2 - 6), \frac{1}{2}(\lambda_\phi^2 - 6), \lambda_\phi^2 - 3\right\}$
p_6	0	0	0	± 1	0	$-3, -3, -3, 0, 0$
p_7	$\frac{\sqrt{3/2}}{\lambda_\phi}$	0	$\pm \frac{\sqrt{3/2}}{\lambda_\phi}$	0	0	$\left\{0, -\frac{3}{2}, \frac{3}{2}, \frac{3(-\lambda_\phi^2 - \sqrt{24\lambda_\phi^2 - 7\lambda_\phi^4})}{4\lambda_\phi^2}, \frac{3(\sqrt{24\lambda_\phi^2 - 7\lambda_\phi^4} - \lambda_\phi^2)}{4\lambda_\phi^2}\right\}$
p_8	$\frac{\lambda_\phi}{\sqrt{6}}$	$\pm \frac{\sqrt{6 - \lambda_\phi^2}}{6}$	0	0	0	$\{0, 0, 0, 3, 3\}$
p_9	$\frac{\lambda_\phi}{\sqrt{6}}$	0	$\pm \frac{\sqrt{6 - \lambda_\phi^2}}{\sqrt{6}}$	0	0	$\left\{0, \frac{\lambda_\phi^2}{2}, \frac{1}{2}(\lambda_\phi^2 - 6), \frac{1}{2}(\lambda_\phi^2 - 6), \lambda_\phi^2 - 3\right\}$

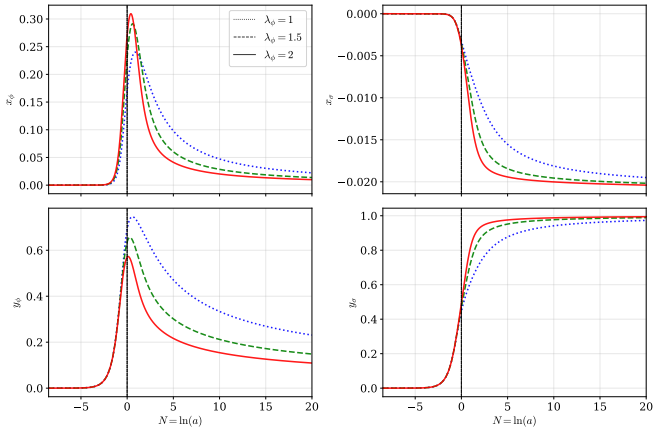
TABLE I: The table of fixed points for the system of equations Eq (20).

Fixed point	Ω_ϕ	Ω_σ	Ω_m	w_{DE}	q
p_1	0	0	1	-1 : $(x_i, y_i \rightarrow 0)$	$\frac{1}{2}$
p_2	0	0	1	-1 : $(x_i, y_i \rightarrow 0)$	$\frac{1}{2}$
p_3	1	0	0	1	2
p_4	$\frac{\sqrt{3/2}}{\lambda_\phi}$	0	$1 - \frac{\sqrt{3/2}}{\lambda_\phi}$	0	$\frac{1}{2}$
p_5	$\frac{\lambda_\phi}{\sqrt{6}}$	0	$1 - \frac{\lambda_\phi}{\sqrt{6}}$	$\frac{\lambda_\phi^2 - 3}{3}$	$-1 + \frac{\lambda_\phi^2}{2}$
p_6	0	1	0	-1	-1
p_7	$\frac{\sqrt{3/2}}{\lambda_\phi}$	0	$1 - \frac{\sqrt{3/2}}{\lambda_\phi}$	0	$\frac{1}{2}$
p_8	$\frac{\sqrt{6}}{\lambda_\phi}$	$\frac{\sqrt{6 - \lambda_\phi^2}}{\lambda_\phi}$	$1 - \left(\frac{\sqrt{6} + \sqrt{6 - \lambda_\phi^2}}{\lambda_\phi}\right)$	1	2
p_9	$\frac{\lambda_\phi}{\sqrt{6}}$	0	$1 - \frac{\lambda_\phi}{\sqrt{6}}$	$\frac{\lambda_\phi^2 - 3}{3}$	$-1 + \frac{\lambda_\phi^2}{2}$

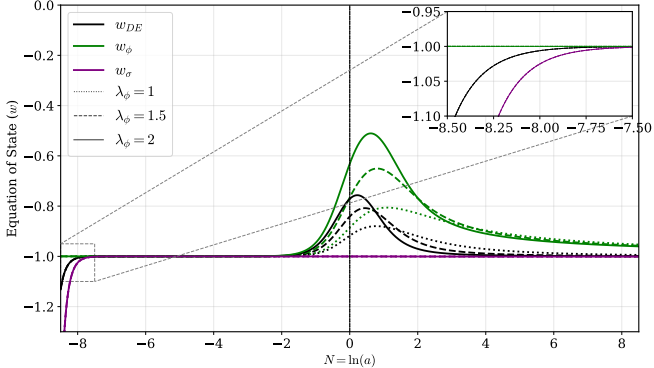
TABLE II: List of fixed Points with their cosmological behaviours.



(a) Evolution of density fractions Ω_m , Ω_r , Ω_{DE} , Ω_ϕ and Ω_σ

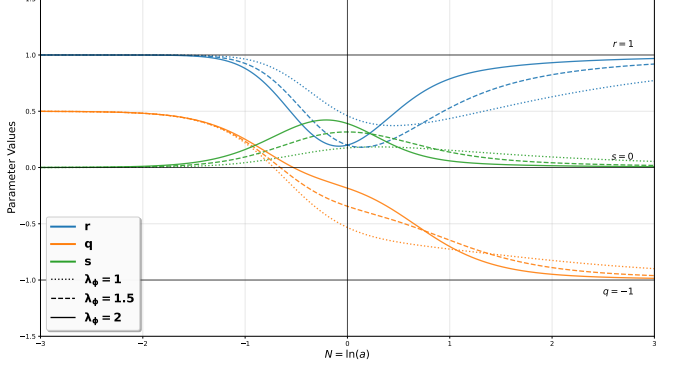


(b) Plot of the evolution of the dimensionless variables x_ϕ (top left), y_ϕ (bottom left), x_σ (top right), y_σ (bottom right).

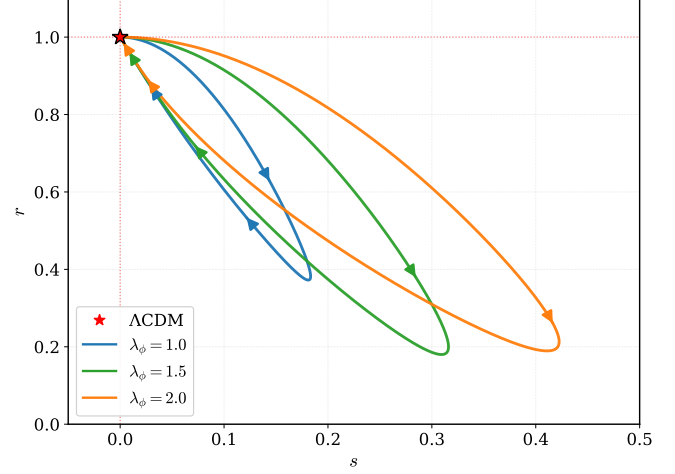


(c) Plot of the equation of state of the scalar fields, quintessence (w_ϕ) in green, phantom (w_σ) in purple and the effective dark energy EoS (w_{DE} in black).

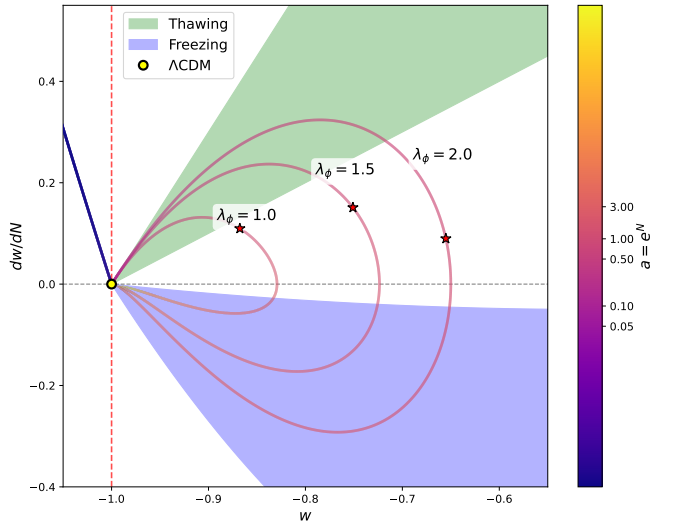
FIG. 2: Plot of different cosmological parameters, density fractions (top panel), dimensionless dynamical system variable (middle panel) and equation of states (bottom panel). The dotted, dashed, solid curves represent $\lambda_\phi = 1, 1.5, 2$ respectively.



(a) The plot of the deceleration parameter (q) in orange, state finder parameter r in blue and the s in green.



(b) Parametric plot of the solutions in the statefinder $r - s$ plane.



(c) The $w'_DE - w_{DE}$ phase space with the present epoch ($a = 1$) represented by the star.

FIG. 3: Plot of different cosmographic and state finder parameters, q, r, s (top panel), $r - s$ phase plot (middle panel) and $\frac{dw}{dN}$ vs w (bottom panel).

The dotted, dashed, solid curves represent $\lambda_\phi = 1, 1.5, 2$ respectively.

ported in earlier studies. Since a cosmological solution starting deep in the radiation-dominated era must transit through this saddle point, the equations of state of both the individual scalar fields and the total dark energy necessarily approach $w \simeq -1$ during matter domination. This behavior is independent of the specific forms of the quintessence and phantom potentials, provided the fields are minimally coupled to gravity and non-interacting at the level of the potential.

Consequently, for any choice of initial conditions with $w_{\text{DE}} \neq -1$ at early times, the system evolves toward $w_{\text{DE}} \simeq -1$ during matter domination and subsequently departs from this value once dark energy becomes dominant. From the dynamical systems perspective, the phantom divide crossing in these types of models is therefore expected to occur asymptotically rather than abruptly.

The evolution of the Hubble parameter $H(N)$ is compared with observational data from cosmic chronometers (see the appendix of Ref. [66]) in Fig. 6, using the same initial conditions as in the previous plots. From the figure, it is evident that the quintom model provides a good fit to the observed Hubble data at late times.

In Fig. 7, we present the differences in BAO distance measures predicted by the quintom model relative to the Λ CDM model, together with the corresponding differences computed from DESI DR2 observations (shown in black). The figure indicates that the quintom model yields a better fit to the BAO data than Λ CDM.

B. State Finder Analysis

To discriminate the model discussed here from other phenomenologically degenerate dark energy scenarios, we perform a statefinder analysis using the diagnostic pair $\{r, s\}$ constructed from the scale factor and its higher-order time derivatives [67, 68]. These parameters are defined as:

$$\{r, s\} \equiv \left\{ \frac{\ddot{a}}{aH^3}, \frac{r-1}{3(q-\frac{1}{2})} \right\}. \quad (26)$$

For an exponentially expanding universe, $a \propto e^t$, one finds, $q = -1$ and $r = 1$, which implies $s = 0$. This corresponds to the late-time behaviour in the Λ CDM model. The evolution of these parameters is

shown in Fig. 3a. Since different dark energy models trace qualitatively distinct trajectories in the $(r-s)$ plane, the statefinder diagnostic provides a tool to distinguish among them. Using Friedmann, acceleration, and conservation equations, we express these parameters in terms of w_i , its time derivatives \dot{w}_i [69]:

$$\begin{aligned} q &= -\frac{\ddot{a}}{aH^2} = \frac{1}{2}(1+3w_i), \\ r &= 1 + \frac{9}{2}(1+w_i)\frac{\dot{p}_i}{\dot{\rho}_i} = 1 + \frac{9}{2}\left(w_i(1+w_i) - \frac{\dot{w}_i}{3H}\right), \\ s &= \frac{(1+w_i)\dot{p}_i}{w_i\dot{\rho}_i} = 1 + w_i - \frac{\dot{w}_i}{3Hw_i}. \end{aligned} \quad (27)$$

Focusing on the late-time dynamics, and noting that the parameter s is ill-defined for pressureless matter, we treat the total dark energy sector as a single effective fluid with equation of state $w_i \equiv w_{\text{DE}}$. Including the radiation component, they can be written as:

$$\begin{aligned} q &= \frac{1}{2}(1+3w_{\text{DE}}\Omega_{\text{DE}} + \Omega_r), \\ r &= 1 + \frac{9\Omega_{\text{DE}}}{2}\left(w_{\text{DE}}(1+w_{\text{DE}}) - \frac{w'_{\text{DE}}}{3}\right) + 2\Omega_r, \\ s &= 1 + w_{\text{DE}}\Omega_{\text{DE}} - \frac{w'_{\text{DE}}}{3w_{\text{DE}}} + \frac{\Omega_r}{3}. \end{aligned} \quad (28)$$

The corresponding trajectories in the $r-s$ plane are displayed in Fig. 3b. The near linearity in the evolution in the past and more pronounced toward the future direction reflects the transition of the deceleration parameter from a matter-dominated phase with $q \simeq 0.5$ to a dark-energy-dominated phase with $q \simeq -1$.

Finally, in Fig. 3c we present the phase-space diagram w'_{DE} vs w_{DE} following the classification introduced in [70]. The green (blue) region corresponds to the thawing (freezing) behaviour of the dark energy equation of state. While canonical quintessence models typically remain confined to one of these regions, quintom models allow for richer dynamics, exhibiting trajectories that go across thawing ($(1+w_{\text{DE}}) < w'_{\text{DE}} < 3(1+w_{\text{DE}})$) and freezing ($3w_{\text{DE}}(1+w_{\text{DE}}) < w'_{\text{DE}} < 0.2w_{\text{DE}}(1+w_{\text{DE}})$) regions at different cosmological epochs.

VI. OBSERVATIONAL DATA

In order to evaluate the performance of this model in relation to contemporary cosmological observations, we analyze several datasets using a Markov Chain Monte Carlo (MCMC) approach implemented with the *COBAYA*[71] package. The background cosmological evolution described by Eq. (20) is implemented in a separate Python module, which is interfaced with *COBAYA* as an external cosmological theory module for the MCMC analysis. In addition, we use the publicly available *GetDist* package to visualize and analyze the resulting posterior distributions.

A. Supernova Data

Standard candles often include Type Ia supernovae due to their notably consistent absolute luminosity [72, 73]. In our current study, we utilized the Pantheon Plus compilation of SN-Ia datasets [7, 74, 75] in conjunction with the DES Year 5 data [76]. These collections are characterized by unique photometric systems and selection approaches, offering distance moduli μ across a span of redshifts.

B. DESI BAO Data

The visible baryonic matter density demonstrates repeating, periodic variations known as baryon acoustic oscillations. These oscillations are crucial standard rulers for accurate cosmological distance measurements. In this work, the 2025 BAO data from the Dark Energy Spectroscopic Instrument (DESI-DR2), as cited in reference [17, 77], have been utilized¹. BAO provides measurements of the effective distance parallel to the line of sight as follows,

$$\frac{D_H(z)}{r_d} = \frac{cr_d^{-1}}{H(z)}, \quad (29)$$

and perpendicular to the line of sight as,

$$\frac{D_M(z)}{r_d} \equiv \frac{c}{r_d} \int_0^z \frac{d\tilde{z}}{H(\tilde{z})} = \frac{c}{H_0 r_d} \int_0^z \frac{d\tilde{z}}{h(\tilde{z})}. \quad (30)$$

¹ The DESI DR2 data used in this analysis can be found in <https://github.com/CobayaSampler>.

The angle-averaged distance is calculated as,

$$\frac{D_V(z)}{r_d} = \left[\frac{czr_d^{-3}d_L^2(z)}{H(z)(1+z)^2} \right]^{\frac{1}{3}}, \quad (31)$$

where $d_L(z)$ represents the luminosity distance.

C. Compressed CMB Likelihood

In addition to late-time distance probes, we incorporate cosmic microwave background (CMB) information using a compressed likelihood that encodes early universe physics in a model independent manner. Following the approach described in Appendix A of Ref. [17], the full CMB power spectrum information is compressed into a correlated Gaussian prior on the parameters $(\theta_*, \omega_b, \omega_{bc})$, where θ_* denotes the angular size of the sound horizon at recombination and $\omega_b \equiv \Omega_b h^2$ and $\omega_{bc} \equiv (\Omega_b + \Omega_c)h^2$ are the physical baryon and total matter densities, respectively. These quantities are tightly constrained by the CMB and can be determined largely independently of assumptions about late-time cosmic evolution by marginalizing over effects such as CMB lensing and the late integrated Sachs–Wolfe effect [78].

This compressed CMB likelihood effectively provides a high-redshift anchor for the background expansion history and captures most of the relevant constraining power of the full CMB likelihood for dark energy studies. In particular, it strongly constrains the matter density, thereby breaking degeneracies present in low-redshift probes such as BAO. As demonstrated in Ref. [17], constraints on evolving dark energy models obtained using this compressed likelihood are highly consistent with those derived from the full CMB likelihood, indicating that the dominant CMB information relevant for background cosmology is retained. We therefore adopt this compressed CMB prior as a robust and computationally efficient alternative to fitting the full CMB power spectra.

We have examined the following three combinations of datasets.

1. Set 1: Pantheon Plus + CMB + DESI DR2,
2. Set 2: DES Y5 + CMB + DESI DR2,
3. Set 3: CMB + DESI DR2.

Parameters	Set 1: Pantheon Plus+CMB+DESI DR2		Set 2: DES Y5+CMB+DESI DR2		Set 3: CMB+DESI DR2	
	Λ CDM	Quintom	Λ CDM	Quintom	Λ CDM	Quintom
H_0	68.28 ± 0.29	67.64 ± 0.40	68.16 ± 0.31	67.25 ± 0.39	68.41 ± 0.31	$67.57^{+0.60}_{-0.54}$
Ω_{b0}	0.04789 ± 0.00032	0.04859 ± 0.00045	0.04801 ± 0.00035	0.04902 ± 0.00045	0.04776 ± 0.00035	$0.04867^{+0.00059}_{-0.00068}$
Ω_{m0}	0.3011 ± 0.0037	0.3098 ± 0.0053	0.3028 ± 0.004	0.3153 ± 0.0053	0.2995 ± 0.004	$0.3109^{+0.0071}_{-0.0084}$
Ω_{DE}	0.6989 ± 0.0037	0.6902 ± 0.0053	0.6972 ± 0.004	0.6847 ± 0.0053	0.7005 ± 0.004	$0.6891^{+0.0084}_{-0.0071}$
$\Omega_{\phi 0}$	—	$0.50^{+0.20}_{-0.16}$	—	$0.517^{+0.18}_{-0.071}$	—	$0.50^{+0.20}_{-0.29}$
Ω_{σ}	—	$0.19^{+0.12}_{-0.22}$	—	$0.168^{+0.089}_{-0.19}$	—	$0.19^{+0.11}_{-0.21}$
w_{DE}	-1	$-0.920^{+0.034}_{-0.045}$	-1	$-0.867^{+0.042}_{-0.058}$	-1	$-0.909^{+0.034}_{-0.087}$
λ_{ϕ}	—	1.3072 ± 0.8062	—	1.5676 ± 0.7580	—	1.3198 ± 0.855
χ^2_{min}	1419.93	1410.86	1663.82	1646.01	13.89	7.88
$\Delta\chi^2_{min}$	0	-9.07	0	-17.81	0	-6.02
AIC	1427.93	1426.86	1671.82	1662.01	21.89	23.88
ΔAIC	0	-1.07	0	-9.81	0	1.98
$ \ln B_{Q\Lambda} $	0	2.419	0	1.360	0	3.713

TABLE III: Mean values and 68% confidence intervals for the cosmological parameters, along with $\Delta\chi^2_{min}$, ΔAIC and MCEvidence analyses, are presented for both the Λ CDM and the quintom model.

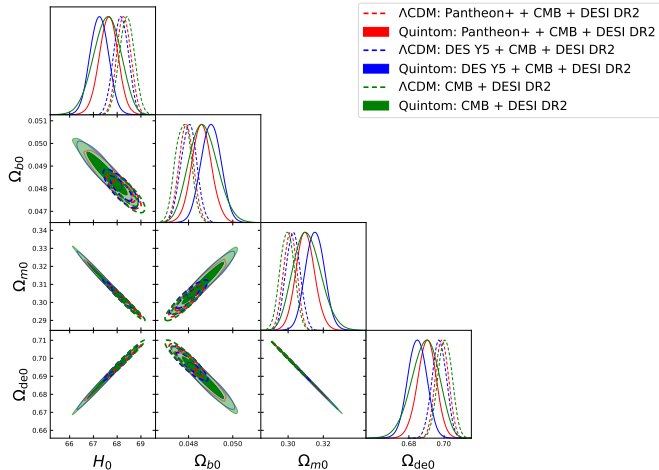


FIG. 4: 1D and 2D triangular plots of the posterior distributions of cosmological parameters for the model and Λ CDM model (dotted) are shown for comparison.

VII. CONSTRAINTS FROM DATA ANALYSIS

In this section, the observational bounds are provided on both the Λ CDM model and the proposed quintom scenario using the combined set of three cosmological data samples mentioned previously. The present-day matter density parameter is defined as $\Omega_m = \Omega_b + \Omega_c$, where Ω_b and Ω_c denote the baryonic and cold dark matter components, respectively. The parameter estimation is performed by imposing flat (uniform) priors on the primary cosmological quantities, namely $H_0 : [60, 80] \text{ km s}^{-1} \text{ Mpc}^{-1}$,

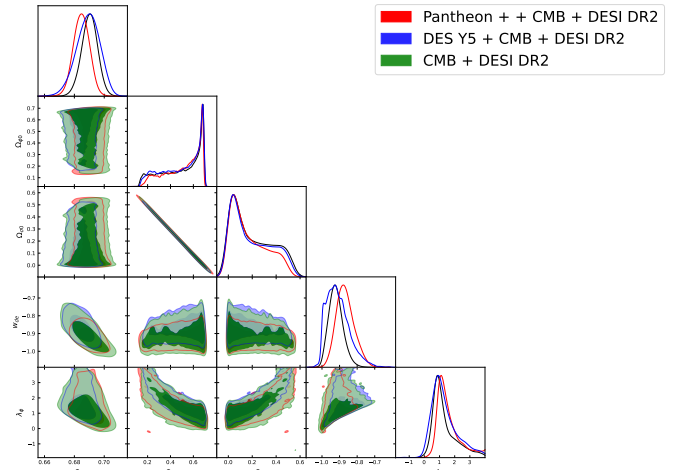


FIG. 5: Triangular plots of the derived cosmological parameters and model parameters for the model.

$\Omega_{b0} : [0.01, 0.1]$ and $\Omega_{m0} : [0.1, 0.5]$. For the quintom sector, additional parameters associated with the dynamical degrees of freedom are allowed to vary within the ranges $x_{\phi 0} \in [0, 0.4]$, $x_{\sigma 0} \in [-0.02, 0.25]$, $y_{\sigma 0} \in [-0.75, 0.75]$, $\lambda_{\phi} \in [-2, 4]$, and $\lambda_{\sigma 0} \in [-2, 2]$, where the subscript “0” denotes present-day values. These parameters encode the initial conditions of the scalar field dynamics as well as the slope of the quintessence potential.

Table III summarizes the best-fit (mean) values together with the corresponding 68% confidence-level limits for both the cosmological and model parameters obtained in our study. These constraints are derived using the three different combinations of observational data sets introduced in the previous

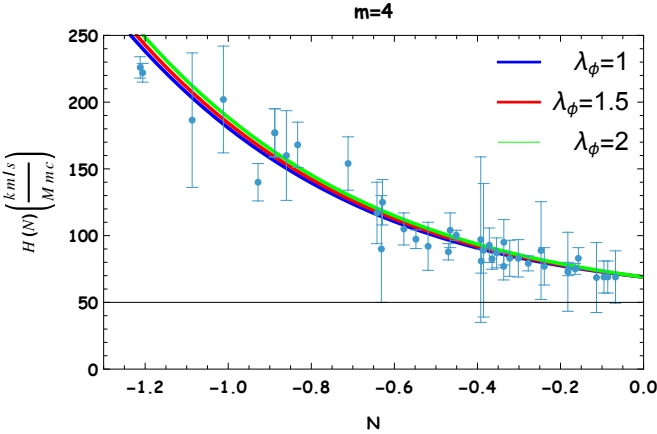


FIG. 6: Evolution of Hubble parameter with observed values.

section. For reference, we also display the results obtained for the standard Λ CDM scenario.

The marginalized one and two-dimensional posterior distributions of the background cosmological parameters H_0 , Ω_{b0} , Ω_{m0} , and Ω_{DE0} are displayed in Fig. 4. The corresponding constraints on the dark-energy sector parameters, including $\Omega_{\phi 0}$, $\Omega_{\sigma 0}$, w_{DE} , and the model parameter λ_ϕ , are shown in Fig. 5. In these figures, the results obtained from data Set 1, Set 2, and Set 3 are represented by red, green, and blue contours, respectively. The Λ CDM constraints are indicated by dotted curves, while solid curves correspond to the quintom model.

Across all three data combinations, the inferred values of the Hubble constant in the quintom scenario are slightly lower than those obtained in the Λ CDM case, although the shifts remain within the 1σ confidence level and therefore do not indicate a statistically significant deviation. The matter density parameter Ω_{m0} is consistently higher in the quintom model, with a corresponding reduction in the dark energy density parameter Ω_{DE0} . This behaviour is a direct consequence of the effective dynamical dark energy equation of state being greater than -1 today for the quintom model.

The decomposition of the dark energy sector reveals that the present cosmic acceleration is predominantly driven by the canonical scalar field, with $\Omega_{\phi 0} \simeq 0.5$, while the phantom component contributes subdominantly, with $\Omega_{\sigma 0} \sim 0.17 - 0.19$ depending on the data set. The total dark energy equation-of-state parameter is constrained to lie in the range $-0.92 \lesssim w_{DE} \lesssim -0.87$, indicating a clear departure from a pure cosmological constant and

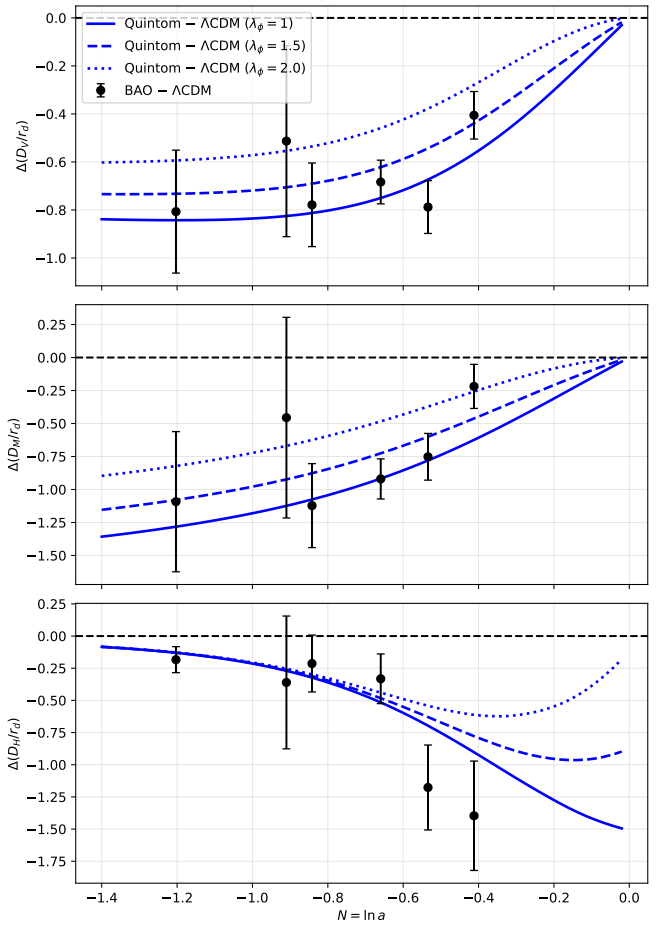


FIG. 7: Plot of BAO distance differences of the quintom model against the Λ CDM model for three different choices of the λ_ϕ parameter. The top panel shows the differences for D_V/r_d , the middle panel is for D_M/r_d and the bottom panel is for D_H/r_d . The difference with the observed data is shown in black points with corresponding error bars.

favouring a dynamical dark energy behaviour.

The relative statistical performance of the quintom model with respect to Λ CDM is quantified using the minimum chi-square value χ^2_{\min} , its difference $\Delta\chi^2_{\min}$, and the Akaike Information Criterion (AIC). As shown in Table III, the quintom model yields lower χ^2_{\min} values for all three data combinations, with the most significant improvement obtained when DES Y5 data are included. This indicates that the extended model provides a better fit to the data at the level of the likelihood.

The difference in the Akaike Information Crite-

tion is defined as

$$\Delta\text{AIC} = \chi_{\min, \mathcal{M}}^2 - \chi_{\min, \Lambda\text{CDM}}^2 + 2(N_{\mathcal{M}} - N_{\Lambda\text{CDM}}), \quad (32)$$

where \mathcal{M} denotes the model under consideration and $N_{\mathcal{M}}$ represents the number of free parameters sampled in the MCMC analysis. A negative value of ΔAIC indicates a preference for the model \mathcal{M} after accounting for its increased complexity.

According to the AIC results reported in Table III, the quintom model is mildly favoured over ΛCDM for the Pantheon Plus+CMB+DESI DR2 data set, and strongly favoured when DES Y5 data are included. In contrast, for the CMB+DESI DR2 combination, the AIC slightly favors the ΛCDM .

In addition to the model comparison based on χ_{\min}^2 and AIC, we also assess the relative performance of the quintom scenario using Bayesian evidence. The Bayesian evidence \mathcal{Z} corresponds to the likelihood integrated over the full parameter space weighted by the prior distributions. In practice, we evaluate the logarithmic Bayes factor between the quintom model and the ΛCDM scenario using the MCEvidence[79] algorithm applied to the MCMC chains.

The resulting values of $\ln B_{Q\Lambda} \equiv \ln(\mathcal{Z}_{\text{Quintom}}/\mathcal{Z}_{\Lambda\text{CDM}})$ are reported in Table III. According to the Jeffreys scale, values of $|\ln B_{Q\Lambda}| \lesssim 1$ indicate inconclusive evidence, values in the range $1 \lesssim |\ln B_{Q\Lambda}| \lesssim 2.5$ correspond to weak evidence, values in the range $2.5 \lesssim |\ln B_{Q\Lambda}| \lesssim 5$ correspond to moderate evidence, values in the range $5 \lesssim |\ln B_{Q\Lambda}| \lesssim 10$ correspond to strong evidence, while values exceeding $|\ln B_{Q\Lambda}| \gtrsim 10$ is interpreted as very strong evidence.

For the datasets including supernova observations (Set 1 and Set 2), the Bayesian evidence analysis indicates a preference for the quintom model over the ΛCDM scenario. Specifically, for Set 1 (Pantheon Plus+CMB+DESI DR2), the Bayes factor $|\ln B_{Q\Lambda}| = 2.419$ provides weak evidence in favor of the quintom model. When considering Set 2 (DES Y5+CMB+DESI DR2), the evidence remains in favor of the quintom model, though at a lower magnitude of $|\ln B_{Q\Lambda}| = 1.360$, suggesting that the improved goodness of fit ($\Delta\chi_{\min}^2 = -17.81$) is balanced against the increased dimensionality of the parameter space. In contrast, for Set 3 (CMB+DESI DR2), the Bayesian evidence $|\ln B_{Q\Lambda}| = 3.713$ moderately favor the Quintom model.

Overall, the Bayesian evidence analysis demon-

strates that while the quintom model provides a significantly better fit to the data in terms of χ_{\min}^2 , achieving improvements of $\Delta\chi^2 = -9.07$ for Set 1 and $\Delta\chi^2 = -17.81$ for Set 2, the current data do not yield decisive Bayesian support over the ΛCDM paradigm. For the datasets including supernova observations, the Bayes factor provides only weak to positive evidence ($1 < |\ln B_{Q\Lambda}| < 3$) for the quintom model, while for Set 3, the evidence actually shifts to favor ΛCDM . This outcome is characteristic of extended dark energy models with additional dynamical degrees of freedom, where the Bayesian evidence penalizes increased model complexity despite the improved fits.

VIII. CONCLUSION

In this work, we have presented a comprehensive study of a quintom dark energy model: a quintessence field with an exponential potential and a phantom degree of freedom governed by an inverse power-law potential. By introducing suitable dimensionless variables, the background equations were cast into an autonomous system, allowing for a systematic classification of the fixed points and their stability properties. The phase space analysis revealed a rich dynamical structure, including matter-dominated saddle points, kinetically dominated early time solutions, and mixed scalar field configurations that can support accelerated expansion. Among all critical points, we identified a unique late-time attractor corresponding to a phantom potential dominated de Sitter phase. Although this attractor is non-hyperbolic, numerical phase space analysis confirms its stability within the physically relevant region, indicating that the model generically evolves toward phantom dominated accelerated expansion at late times.

An important outcome of this analysis is that the cosmological evolution does not proceed directly toward the asymptotic phantom-dominated attractor. Instead, the universe undergoes an intermediate epoch in which the canonical scalar field dominates the dark energy sector including the current epoch, while the phantom component remains subdominant. The effective dark energy equation of state remains close to $w \simeq -1$ throughout the matter-dominated era and subsequently evolves toward less negative values at low redshift, exhibiting a thawing-like behaviour. Both the fields becomes dynamically

relevant only at later times, eventually driving the universe toward the complete phantom domination.

In this model, phantom crossing is achieved by setting the initial conditions within the phantom region during the radiation-dominated epoch. A notable feature of the phantom crossing obtained here is that the crossing of the $w \simeq -1$ barrier occurs gradually and asymptotically, rather than abruptly. Using the dynamical systems framework, we demonstrate that this behaviour of phantom crossing is generic for this class of quintom models in which the scalar fields are not coupled at the level of the potential.

We confronted the model with current cosmological observations using several combinations of low and high-redshift data, including Type Ia supernovae, cosmic microwave background distance priors and baryon acoustic oscillations. The results show

that the quintom scenario provides a fit to the data that is at least comparable to that of the standard Λ CDM model and, in some data combinations, leads to a modest improvement in the minimum χ^2 . Information criteria analyses indicate that the statistical preference for the quintom model is dataset dependent, with mild to moderate support.

ACKNOWLEDGEMENT

PHP acknowledges financial support from *Fundaão de Amparo à pesquisa e Inovação do Espírito Santo* (FAPES, Brazil) and is grateful to the Departamento de Física Teórica, UERJ and the ITA, University of Oslo, for their hospitality. Authors are also thanful to L. Arturo Ureña-López for helping with the implementation of compresed CMB likelihood in *COBAYA*.

[1] N. Aghanim et al. Planck 2018 results. VI. Cosmological parameters. *Astron. Astrophys.*, 641:A6, 2020. [Erratum: *Astron. Astrophys.* 652, C4 (2021)].

[2] Shadab Alam, Metin Ata, Stephen Bailey, Florian Beutler, Dmitry Bizyaev, Jonathan A. Blazek, Adam S. Bolton, Joel R. Brownstein, Angela Burden, Chia-Hsun Chuang, and et al. The clustering of galaxies in the completed sdss-iii baryon oscillation spectroscopic survey: cosmological analysis of the dr12 galaxy sample. *Monthly Notices of the Royal Astronomical Society*, 470(3):2617–2652, Mar 2017.

[3] Shadab Alam, Marie Aubert, Santiago Avila, Christophe Balland, Julian E. Bautista, Matthew A. Bershadsky, Dmitry Bizyaev, Michael R. Blanton, Adam S. Bolton, Jo Bovy, and et al. Completed sdss-iv extended baryon oscillation spectroscopic survey: Cosmological implications from two decades of spectroscopic surveys at the apache point observatory. *Physical Review D*, 103(8), Apr 2021.

[4] T. M. C. Abbott et al. Dark Energy Survey year 1 results: Cosmological constraints from galaxy clustering and weak lensing. *Phys. Rev. D*, 98(4):043526, 2018.

[5] Adam G. Riess, Stefano Casertano, Wenlong Yuan, Lucas M. Macri, and Dan Scolnic. Large magellanic cloud cepheid standards provide a 1% foundation for the determination of the hubble constant and stronger evidence for physics beyond Λ cdm. *The Astrophysical Journal*, 876(1):85, May 2019.

[6] Kenneth C. Wong et al. H0LiCOW – XIII. A 2.4 percent measurement of H0 from lensed quasars: 5.3 σ tension between early- and late-Universe probes. *Mon. Not. Roy. Astron. Soc.*, 498(1):1420–1439, 2020.

[7] Adam G. Riess, Louise Breuval, Wenlong Yuan, Stefano Casertano, Lucas M. Macri, J. Bradley Bowers, Dan Scolnic, Tristan Cantat-Gaudin, Richard I. Anderson, and Mauricio Cruz Reyes. Cluster cepheids with high precision gaia parallaxes, low zero-point uncertainties, and hubble space telescope photometry. *The Astrophysical Journal*, 938(1):36, oct 2022.

[8] Théo Simon, Pierre Zhang, Vivian Poulin, and Tristan L. Smith. Consistency of effective field theory analyses of the BOSS power spectrum. *Phys. Rev. D*, 107(12):123530, 2023.

[9] Sihan Yuan, Lehman H. Garrison, Daniel J. Eisenstein, and Risa H. Wechsler. Stringent σ_8 constraints from small-scale galaxy clustering using a hybrid MCMC + emulator framework. *Mon. Not. Roy. Astron. Soc.*, 515(1):871–896, 2022.

[10] L. F. Secco et al. Dark Energy Survey Year 3 results: Cosmology from cosmic shear and robustness to modeling uncertainty. *Phys. Rev. D*, 105(2):023515, 2022.

[11] J. L. van den Busch et al. KiDS-1000: Cosmic shear with enhanced redshift calibration. *Astron. Astrophys.*, 664:A170, 2022.

[12] Angus H. Wright et al. KiDS-Legacy: Cosmological constraints from cosmic shear with the complete Kilo-Degree Survey. *Astron. Astrophys.*, 703:A158, 2025.

[13] P. A. R. Ade et al. Planck 2015 results. XXIV. Cosmology from Sunyaev-Zeldovich cluster counts. *Astron. Astrophys.*, 594:A24, 2016.

[14] A. G. Adame et al. DESI 2024 VII: cosmological constraints from the full-shape modeling of clustering measurements. *JCAP*, 07:028, 2025.

[15] R. Calderon et al. DESI 2024: Reconstructing Dark Energy using Crossing Statistics with DESI DR1 BAO data. 5 2024.

[16] A. G. Adame et al. DESI 2024 III: Baryon Acoustic Oscillations from Galaxies and Quasars. 4 2024.

[17] M. Abdul Karim et al. DESI DR2 Results II: Measurements of Baryon Acoustic Oscillations and Cosmological Constraints. 3 2025.

[18] K. Lodha et al. Extended dark energy analysis using DESI DR2 BAO measurements. *Phys. Rev. D*, 112(8):083511, 2025.

[19] S. Filbert et al. Broad absorption line quasars in the Dark Energy Spectroscopic Instrument Early Data Release. *Mon. Not. Roy. Astron. Soc.*, 532(4):3669–3681, 2024.

[20] M. Ishak, J. Pan, R. Calderon, K. Lodha, G. Valogiannis, A. Aviles, G. Niz, L. Yi, C. Zheng, C. Garcia-Quintero, et al. Modified gravity constraints from the full shape modeling of clustering measurements from desi 2024. *Journal of Cosmology and Astroparticle Physics*, 2025(09):053, September 2025.

[21] Marina Cortês and Andrew R. Liddle. Interpreting DESI's evidence for evolving dark energy. *JCAP*, 12:007, 2024.

[22] Nandan Roy and Soumya Chakrabarti. Is Phantom Barrier Crossing Inevitable? A Cosmographic Analysis. 8 2025.

[23] Nandan Roy. Dynamical dark energy in the light of DESI 2024 data. 6 2024.

[24] David Shlivko and Paul J. Steinhardt. Assessing observational constraints on dark energy. *Physics Letters B*, 855:138826, 2024.

[25] William J. Wolf and Pedro G. Ferreira. Underdetermination of dark energy. *Phys. Rev. D*, 108(10):103519, 2023.

[26] David Shlivko and Paul J. Steinhardt. Assessing observational constraints on dark energy. *Phys. Lett. B*, 855:138826, 2024.

[27] William J. Wolf, Carlos García-García, Deaglan J. Bartlett, and Pedro G. Ferreira. Scant evidence for thawing quintessence. *Phys. Rev. D*, 110(8):083528, 2024.

[28] Emanuely Silva and Rafael C. Nunes. Testing signatures of phantom crossing through full-shape galaxy clustering analysis. *JCAP*, 11:078, 2025.

[29] Zhiyu Lu, Théo Simon, and Pierre Zhang. Preference for evolving dark energy in light of the galaxy bispectrum. 3 2025.

[30] Alex González-Fuentes and Adrià Gómez-Valent. Reconstruction of dark energy and late-time cosmic expansion using the Weighted Function Regression method. *JCAP*, 12:049, 2025.

[31] Ryan E. Keeley, Arman Shafieloo, and William L. Matthewson. Could We Be Fooled about Phantom Crossing? 6 2025.

[32] Vrund Patel, Amlan Chakraborty, and Luca Amendola. The prior dependence of the DESI results. 7 2024.

[33] Bo Feng, Xiu-Lian Wang, and Xin-Min Zhang. Dark energy constraints from the cosmic age and supernova. *Phys. Lett. B*, 607:35–41, 2005.

[34] Zong-Kuan Guo, Yun-Song Piao, Xin-Min Zhang, and Yuan-Zhong Zhang. Cosmological evolution of a quintom model of dark energy. *Phys. Lett. B*, 608:177–182, 2005.

[35] Gong-Bo Zhao, Jun-Qing Xia, Mingzhe Li, Bo Feng, and Xinmin Zhang. Perturbations of the quintom models of dark energy and the effects on observations. *Phys. Rev. D*, 72:123515, 2005.

[36] Wen Zhao and Yang-Hong Zhang. Quintom models with an equation of state crossing -1. *Physical Review D*, 73:123509, 2006.

[37] L. W. K. Goh and A. N. Taylor. Phantom Crossing with Quintom Models. *Mon. Not. Roy. Astron. Soc.*, 3142:3157, 2025.

[38] Yi-Fu Cai, Emmanuel N. Saridakis, Mohammad R. Setare, and Jun-Qing Xia. Quintom Cosmology: Theoretical implications and observations. *Phys. Rept.*, 493:1–60, 2010.

[39] Yi-Fu Cai, Xin Ren, Taotao Qiu, Mingzhe Li, and Xinmin Zhang. The quintom theory of dark energy after desi dr2. 2025. arXiv preprint, to appear.

[40] Jun-Xian Li and Shuang Wang. Reconstructing dark energy with model independent methods after desi dr2 bao. 2025. arXiv preprint, to appear.

[41] Yuhang Yang, Qingqing Wang, Xin Ren, E. Saridakis, and Yi-Fu Cai. Modified gravity realizations of quintom dark energy after desi dr2. 2025. arXiv preprint, to appear.

[42] Yuichiro Tada and Takahiro Terada. Quintessential interpretation of the evolving dark energy in light of desi observations. *Physical Review D*, 109(8):083520, 2024.

[43] Yuhang Yang, Xin Ren, Qingqing Wang, Zhiyu Lu, Dongdong Zhang, Yi-Fu Cai, and E. Saridakis. Quintom cosmology and modified gravity after desi 2024. *Science Bulletin*, 69(24):2698–2705, 2024.

[44] Ioannis D. Gialamas, Gert Hütsi, Martti Raidal, Juan Urrutia, Martin Vasar, and Hardi Veermäe. Quintessence and phantoms in light of DESI 2025. *Phys. Rev. D*, 112(6):063551, 2025.

[45] Adrià Gómez-Valent and Alex González-Fuentes. Effective phantom divide crossing with standard and negative quintessence. *Phys. Lett. B*, 872:140096, 2026.

[46] C. Armendariz-Picon, V. Mukhanov, and P. J. Steinhardt. k-essence as a model for dark energy. *Physical Review Letters*, 85(15):4438–4441, 2001.

[47] Sourav Sur and Saurya Das. Multiple kinetic k-essence, phantom barrier crossing and stability. *JCAP*, 01:007, 2009.

[48] Rio Saitou and Shin'ichi Nojiri. Stable phantom-divide crossing in two scalar models with matter. *Eur. Phys. J. C*, 72:1946, 2012.

[49] Jiro Matsumoto. Phantom crossing dark energy in Horndeski's theory. *Phys. Rev. D*, 97(12):123538, 2018.

[50] Hao Wei, Rong-Gen Cai, and Ding-Fang Zeng. Hesse: A New view of quintom dark energy. *Class. Quant. Grav.*, 22:3189–3202, 2005.

[51] Shao-Feng Wu, Auttakit Chatrabhuti, Guo-Hong Yang, and Peng-Ming Zhang. Crossing the phantom divide in brane cosmology with curvature corrections and brane-bulk energy transfer. *Phys. Lett. B*, 659:45–53, 2008.

[52] Kazuharu Bamba, Chao-Qiang Geng, and Chung-Chi Lee. Phantom crossing in viable $f(R)$ theories. *Int. J. Mod. Phys. D*, 20:1339–1345, 2011.

[53] Shin'ichi Nojiri, S. D. Odintsov, and V. K. Oikonomou. Phantom crossing and oscillating dark energy with $F(R)$ gravity. *Phys. Rev. D*, 112(10):104035, 2025.

[54] Nandan Roy and Kazuharu Bamba. Arbitrariness of potentials in interacting quintessence models. *Phys. Rev. D*, 99(12):123520, 2019.

[55] Chonticha Kritpetch, Nandan Roy, and Narayan Banerjee. Interacting dark sector: A dynamical system perspective. *Phys. Rev. D*, 111(10):103501, 2025.

[56] Prasanta Sahoo, Nandan Roy, and Himadri Shekhar Mondal. Constraint on Momentum-coupled Dark Energy using DESI DR2. 6 2025.

[57] David Andriot. Quintessence: An Analytical Study, With Theoretical and Observational Applications. *Fortsch. Phys.*, 73(6):e70007, 2025.

[58] David Andriot. Phantom matters. *Phys. Dark Univ.*, 49:102000, 2025.

[59] Francisco X. Linares Cedeño, Nandan Roy, and L. Arturo Ureña López. Tracker phantom field and a cosmological constant: Dynamics of a composite dark energy model. *Phys. Rev. D*, 104(12):123502, 2021.

[60] Emmanuel N. Saridakis. Phantom evolution in power-law potentials. *Nucl. Phys.*, B819:116–126, 2009.

[61] P. Binetruy. Models of dynamical supersymmetry breaking and quintessence. *Phys. Rev. D*, 60:063502, 1999.

[62] A. Masiero, M. Pietroni, and F. Rosati. Susy qcd and quintessence. *Phys. Rev. D*, 61:023504, Dec 1999.

[63] Chung-Pei Ma and Edmund Bertschinger. Cosmological perturbation theory in the synchronous and conformal Newtonian gauges. *Astrophys. J.*, 455:7–25, 1995.

[64] Sebastian Bahamonde, Christian G. Böhmer, Sante Carloni, Edmund J. Copeland, Wei Fang, and Nicola Tamanini. Dynamical systems applied to cosmology: dark energy and modified gravity. *Phys. Rept.*, 775–777:1–122, 2018.

[65] Nandan Roy and L. Arturo Ureña López. Tracker behaviour of quintom dark energy and the Hubble tension. 12 2023.

[66] Prasanta Sahoo, Nandan Roy, and Himadri Shekhar Mondal. Quintessence scalar field and cosmological constant: dynamics of a multi-component dark energy model. *Gen. Rel. Grav.*, 57(2):38, 2025.

[67] Takeshi Chiba and Takashi Nakamura. The Luminosity distance, the equation of state, and the geometry of the universe. *Prog. Theor. Phys.*, 100:1077–1082, 1998.

[68] Varun Sahni, Tarun Deep Saini, Alexei A. Starobinsky, and Ujjaini Alam. Statefinder: A New geometrical diagnostic of dark energy. *JETP Lett.*, 77:201–206, 2003.

[69] Pu-xun Wu and Hong-wei Yu. Statefinder parameters for quintom dark energy model. *Int. J. Mod. Phys. D*, 14:1873–1882, 2005.

[70] R. R. Caldwell and Eric V. Linder. The Limits of quintessence. *Phys. Rev. Lett.*, 95:141301, 2005.

[71] Jesus Torrado and Antony Lewis. Cobaya: Code for Bayesian Analysis of hierarchical physical models. *JCAP*, 05:057, 2021.

[72] AG Riess et al. Supernova serach team. *Astron. J.*, 116:1009, 1998.

[73] Adam G. Riess et al. Observational evidence from supernovae for an accelerating universe and a cosmological constant. *Astron. J.*, 116:1009–1038, 1998.

[74] Dan Scolnic et al. The Pantheon+ Analysis: The Full Data Set and Light-curve Release. *Astrophys. J.*, 938(2):113, 2022.

[75] Dillon Brout et al. The Pantheon+ Analysis: Cosmological Constraints. *Astrophys. J.*, 938(2):110, 2022.

[76] T. M. C. Abbott et al. The Dark Energy Survey: Cosmology Results with ~ 1500 New High-redshift Type Ia Supernovae Using the Full 5 yr Data Set. *Astrophys. J. Lett.*, 973(1):L14, 2024.

[77] A. G. Adame et al. DESI 2024 VI: Cosmological Constraints from the Measurements of Baryon Acoustic Oscillations. 4 2024.

[78] Pablo Lemos and Antony Lewis. CMB constraints on the early Universe independent of late-time cosmology. *Phys. Rev. D*, 107(10):103505, 2023.

[79] Alan Heavens, Yabebal Fantaye, Arrykrishna Mootoovaloo, Hans Eggers, Zafirah Hosenie, Steve Kroon, and Elena Sellentin. Marginal Likelihoods from Monte Carlo Markov Chains. 4 2017.